

A Transition Mass in the Local Tully-Fisher Relation

Raymond C. Simons^{1*}, Susan A. Kassin², Benjamin J. Weiner³, Timothy M. Heckman¹,
Janice C. Lee², Jennifer M. Lotz², Michael Peth¹ and Kirill Tchernyshyov¹

¹*Johns Hopkins University, Baltimore, MD*

²*Space Telescope Science Institute, 3700 San Martin Drive, Baltimore, MD*

³*Steward Observatory, University of Arizona, Tucson, AZ*

Accepted ??, Received ??; in original form ??

ABSTRACT

We study the stellar mass Tully-Fisher relation (TFR; stellar mass versus rotation velocity) for a morphologically blind selection of emission line galaxies in the field at redshifts $0.1 < z < 0.375$. Kinematics (σ_g , V_{rot}) are measured from emission lines in Keck/DEIMOS spectra and quantitative morphology is measured from V- and I-band Hubble images. We find a transition stellar mass in the TFR, $\log M_* = 9.5 M_\odot$. Above this mass, nearly all galaxies are rotation-dominated, on average more morphologically disk-like according to quantitative morphology, and lie on a relatively tight TFR. Below this mass, the TFR has significant scatter to low rotation velocity and galaxies can either be rotation-dominated disks on the TFR or asymmetric or compact galaxies which scatter off. We refer to this transition mass as the “mass of disk formation”, M_{df} because above it all star-forming galaxies form disks (except for a small number of major mergers and highly star-forming systems), whereas below it a galaxy may or may not form a disk.

Key words: galaxies: evolution - galaxies: formation - galaxies: fundamental parameters - galaxies: kinematics and dynamics

1 INTRODUCTION

The Tully-Fisher relation (TFR; Tully & Fisher 1977) is an empirical scaling between the luminosity of a disk galaxy and its rotation velocity. Later work replaced luminosity with the more physical quantity stellar mass, M_* . In the local Universe, the TFR is remarkably tight (Verheijen 2001; Bell & de Jong 2001; Pizagno et al. 2005; Kassin et al. 2006; Courteau et al. 2007; Masters et al. 2008; Reyes et al. 2011) and its parameterization serves as an important constraint for models of disk galaxy formation (e.g. Mo et al. 1998; Somerville & Primack 1999; Navarro & Steinmetz 2000; Dutton et al. 2007).

Although the TFR is well behaved for ordered disk galaxies, morphologically disturbed or compact galaxies tend to fall below the local relation, exhibiting low rotation velocity for a given stellar mass (Kassin et al. 2007, 2012). Ordered velocity fields may be disturbed in major

merging events or tidal disruptions (Rampazzo et al. 2005; Kronberger et al. 2007; Covington et al. 2010; De Rossi et al. 2012), through the accretion of non-ordered external angular momentum from cold flows (Brooks et al. 2009; Elmegreen & Burkert 2010) and/or disruptive feedback (Mac Low & Ferrara 1999; Lehnert et al. 2009).

Weiner et al. (2006b) and Kassin et al. (2007) demonstrated that accounting for both the disordered motions (σ_g) and ordered rotation velocity (V_{rot}) in a new kinematic quantity, $S_{0.5} = \sqrt{0.5V_{rot}^2 + \sigma_g^2}$, re-establishes a tighter $S_{0.5}$ - M_* scaling relation. This relation is independent of galaxy morphology and coincident with the Faber-Jackson relation for early type galaxies. Numerical simulations have shown that $S_{0.5}$ traces the overall potential well of galaxy-dark halo systems, even for galaxies undergoing drastic kinematic events, such as a major merger (Covington et al. 2010). The measurement of a disordered velocity component has been incorporated more in recent years (e.g. Förster Schreiber et al. 2009; Puech et al. 2010; Lemoine-Busserolle & Lamareille

* E-mail: rsimons@jhu.edu

2010; Catinella et al. 2012; Vergani et al. 2012; Cortese et al. 2014; Wisnioski et al. 2015).

With further investigation, Kassin et al. (2012) demonstrated that since $z \sim 1$ star-forming galaxies have been kinematically settling from systems with a dominant dispersion component to rotationally supported disks. Such galaxies follow kinematic downsizing: more massive galaxies exhibit the most ordered kinematics (high V_{rot}/σ_g) at all epochs. While high and intermediate mass galaxies are likely settling to disks, it is unclear whether low mass galaxies follow the same evolutionary path.

It is well known locally that morphological type is a strong function of stellar mass, with dwarf systems exhibiting more irregular morphology, distinct from their large disk counterparts (e.g. Roberts & Haynes 1994; Bothwell et al. 2009; Mahajan et al. 2015). Moreover, there is mounting evidence that disturbed galaxies are increasingly more common at low masses in the early Universe (Mortlock et al. 2013).

However, kinematic surveys often select against galaxies with disturbed morphologies with regards to other interests, e.g. performing distance measurements or studying dark matter (e.g. Bershadsky et al. 2010). In the local Universe, dwarf galaxies can show rotational signatures in both their HI and stellar components (e.g. Swaters et al. 2002, 2009; McConnachie 2012). When the morphological selection is opened to include irregular galaxies, compact galaxies, and close pairs, the presence of features such as peculiar velocity fields and thick disks are found. Indeed, complex kinematics and low rotational support is frequently found for both low luminosity (e.g. Barton et al. 2001; Kannappan et al. 2002; Young et al. 2003; Vaduvescu et al. 2005; Kirby et al. 2014; Cortese et al. 2014) and highly star-forming dwarfs (e.g. van Zee et al. 1998; Cannon et al. 2004; Lelli et al. 2014). However, locally, limited studies have been performed placing large samples of these disordered systems on the TFR, or relating the relative contributions of V and σ to the morphology of the galaxy.

In this paper we study the resolved kinematics for a morphologically unbiased sample of star-forming galaxies at $z \sim 0.2$. Compared to nearby samples, a survey at $z \sim 0.2$ benefits from the smaller angular sizes of galaxies and the higher target density. Large homogenous samples can be efficiently obtained with a multi-object spectrograph. This sample is unique from other local samples in that we include galaxies with both disturbed and disk-like morphologies. Furthermore, we incorporate measurements of the non-negligible contributions from random motions as well as the rotation velocity.

In section 2, we discuss the sample selection, the method used for measuring kinematics from emission lines and the measurements of quantitative morphologies. In section 3, we present the main result of this paper: a transition stellar mass in the TFR. In section 4, we illustrate the correlation between gas phase kinematics and galaxy morphology. In section 5, we compare our results with measurements of kinematics for low mass galaxies in the literature both locally and at intermediate redshift. Our conclusions are presented in section 6. In the Appendix, we test our ability to

recover kinematics for the galaxies with the smallest angular extent in our sample. We adopt a Λ CDM cosmology defined with $(h, \Omega_m, \Omega_\Lambda) = (0.7, 0.3, 0.7)$.

2 DATA AND SAMPLE SELECTION

In this section we detail the sample selection and the measurements of the kinematics and morphological indices. We reference the Appendix for further analysis and discussion of the effects of seeing on our kinematic measurements.

We focus on the lowest redshift bin in the galaxy sample used by Kassin et al. (2007) and Kassin et al. (2012) (hereafter referred to as K07 and K12, respectively), namely $0.1 < z < 0.375$. At these redshifts, the K12 sample is sensitive to low mass dwarf galaxies. We briefly review how this sample was selected and defer to K12 for further details. The K12 sample is drawn from field 1 of the DEEP2 Redshift Survey (Newman et al. 2013). DEEP2 employed the DEIMOS multi-object spectrograph (Faber et al. 2003) on the Keck-II telescope. The 1200 line/mm grating was used and the slits were fixed at $1''$, leading to a spectral resolution of $R \sim 5000$. The K12 sample was cut on nebular line strength ($> 10^{-17} \text{ erg s}^{-1} \text{ cm}^{-2}$), available Hubble Space Telescope (HST) imaging and slit alignment from the photometric major axis ($\leq 40^\circ$).

We use HST imaging in two passbands with the Advanced Camera for Surveys (ACS), V (F606W) and I (F814W), from the AEGIS survey (Davis et al. 2007). Each of the images has a pixel scale of $0.03''$ and a typical FWHM PSF of $0.1''$ (0.33 kpc at $z = 0.2$). Inclinations are measured with the SExtractor software (Bertin & Arnouts 1996) using the V-band HST image. The V-band traces the young stars and thus should not be very different from the nebular emission line morphology. A further cut is applied to the sample, limiting inclinations to $30^\circ < i < 70^\circ$, to avoid uncertain inclination corrections for face-on galaxies and dust effects in edge on systems. However, a handful (4) of severely disturbed galaxies for which inclinations and PAs are uncertain are included. The exclusion of these galaxies does not alter our conclusions.

Stellar masses were derived using the rest frame B-V color and absolute B-band magnitude (Bell & de Jong 2001; Bell et al. 2005) with refined empirical corrections from SED fitting (Bundy et al. 2006), as described in Lin et al. (2007). The adopted IMF is from Chabrier (2003). Errors on stellar masses are approximately 0.2 dex.

Spectral slits must be aligned to within 40° of a galaxy's major axis to reliably recover rotation (Weiner et al. 2006a). K07 removed galaxies with slits misaligned by more than 40° from the HST derived photometric major axis, except for the 4 galaxies with severely disturbed morphologies. Beyond this cut there are no residual correlations between measured kinematics (rotation or dispersion) and slit alignment in our sample. The scale of the atmospheric turbulence sets a limiting angular size for measuring rotation velocity in a galaxy. The seeing tends to smooth and eliminate small scale rotation gradients. We test the limiting resolving power imposed

by beam smearing in the Appendix. For the observational conditions of DEEP2 and for the lowest S/N in our sample, kinematics can be measured for galaxies to diameters encompassing 95% of the light (D_{95}) of $(0.87 \pm 0.06) \times$ seeing. We make a further cut on the K07 sample and remove 12 galaxies which are not extended enough to confidently measure kinematics.

Our final sample contains 119 galaxies and uniformly covers the “blue cloud” (Figure 1 in K12). The qualifying feature of our selection is that, aside from the inclination cut, there was no explicit selection on morphology. Contrary to previous TFR studies, this sample selection includes disturbed and compact galaxies. This allows us to more fully sample the population of emission line galaxies.

2.1 Kinematics

We adopt kinematics measured from bright nebular emission lines ($H\alpha$ $\lambda 6563$ or $[OIII]$ $\lambda 5007$) in K07. The rotation velocity, uncorrected for inclination, and spatially resolved gas dispersion, σ_g , were measured with the program ROTCURVE (Weiner et al. 2006a), taking into account the effects of seeing. The seeing was measured through alignment stars on each slit mask (see Newman et al. 2013). For our sample, the seeing varied between $0.55''$ and $1.2''$ FWHM, with a median value of $0.75''$ (1.36 kpc at $z = 0.1$, 3.84 kpc at $z = 0.375$).

The kinematic measurements have been described in previous papers, so we will briefly review them here and refer to Weiner et al. (2006a) for the details. In short, ROTCURVE builds model arctan rotation curves where V is the velocity on the flat part of the rotation curve ($V_{rot} \times \sin(i)$), with an additional dispersion term (σ_g), which is constant with radius. Due to the seeing, the rise of the rotation curve is not well resolved and the turnover radius for the rotation curve (r_t) is not well constrained. The turnover radius is kept fixed to a value of $0.2''$. The recovered rotation velocity and turnover radius are only slightly covariant, with a marginal ± 0.1 dex change in V for a $\pm 0.1''$ change in r_t . Models with varying V and σ_g are blurred with the seeing and fit to the data. V and σ_g are explored with a grid spacing of 5 km s^{-1} and the best fit value is determined through a χ^2 minimization on this grid.

The spectral resolution of the 1200 line/mm grating used by the DEEP2 survey allows measurements for $V_{rot} \times \sin(i)$ down to $\sim 5 \text{ km s}^{-1}$ and σ_g to $\sim 15 \text{ km s}^{-1}$. Measurements with best fits below these limitations are set to these values as upper limits. This is the case for 7 galaxies for V_{rot} and 22 galaxies for σ_g . Example kinematic fits and the corresponding χ^2 spaces are shown later in this paper in Figure 4.

HST imaging is used to measure inclinations in order to correct the measured rotation velocity. As mentioned previously, corrections were not applied to four galaxies with severely disturbed morphologies where the inclination was highly uncertain. They are marked with carets in Figure 1.

We note that the quantity σ_g is *not* like the typical pressure supported velocity dispersion measured from stel-

lar absorption lines in early-type galaxies. Since σ_g is tracing hot gas which can radiate, a high dispersion system can not remain in equilibrium after a crossing time. Therefore σ_g is effectively measuring velocity gradients below the seeing limit, as illustrated by the simulations of Covington et al. 2010. The typical thermal broadening for $T \sim 10^4 \text{ K}$ Hydrogen gas is 10 km s^{-1} , so a measure of $\sigma_g > 25 \text{ km s}^{-1}$ is tracing the relative motions of HII regions and/or disordered motions associated with unresolved velocity gradients (Weiner et al. 2006a, K12).

2.2 Quantitative Morphology

High resolution HST-ACS images allow us to quantify morphologies for each galaxy. In particular, we examine three indices: the Gini coefficient, asymmetry, and concentration. We find little difference between the indices for the V- and I-band and so we simply adopt the I-band measurements (approximately rest V-band at $z=0.2$) for our analysis. We describe these parameters now and examine how they correlate with kinematics in section 4.

The Gini coefficient was adopted from economic theory. As applied to the study of galaxy morphology, the Gini coefficient provides a non-parametric measurement of the distribution of light among the pixels associated with a galaxy (Abraham et al. 2003; Lotz et al. 2004). The Gini coefficient approaches unity for systems with a large fraction of intensity confined to only a few pixels and approaches zero for a uniform intensity distribution. It compliments the more standard concentration index (Abraham et al. 1994), as both trace intensity clustering, but the Gini coefficient is insensitive to the location of the clustering. The typical uncertainty on the Gini coefficient is 0.02, as determined from empirical comparisons of deep (UDF) and shallow fields (GOODS) (Lotz et al. 2006).

The concentration index (defined in e.g. Abraham et al. 1994 and Simard et al. 2002) measures the ratio of flux contained in two isophotes. The outer isophote is defined by the 2σ background contour with a normalized radius of 1 and the inner isophote is defined by a normalized radii of α . Concentration, asymmetry, and size were measured with the GIM2D software (Simard et al. 2002), which simultaneously fit to both the V- and I-band images. The concentration index is measured for $\alpha = (0.1, 0.2, 0.3, 0.4)$. We find no significant differences in trends between alpha levels and adopt $\alpha = 0.1$ for our analysis.

The asymmetry index in GIM2D is as defined in Abraham et al. (1994, 1996). Asymmetry is measured by first assigning contiguous pixels to the galaxy, rotating the image by 180° and then self-subtracting the mirrored image from the original image.

The error bars we use in the figures below for asymmetry and concentration represent the typical 1σ scatter between the four GIM2D measurements for each individual V-Band image. These do not represent the additional uncertainty from the image S/N (limiting magnitude $\sim 28.7 \text{ AB}$), for which comparisons with deeper fields are needed. Shallower studies than ours (limiting magnitude $\sim 26.5 \text{ AB}$;

e.g. Peth et al. 2015) find relative uncertainties in Concentration and Asymmetry of ~ 0.05 with respect to deeper data (limiting magnitude ~ 27.4 AB).

3 A TRANSITION MASS IN THE TFR, THE MASS OF DISK FORMATION (M_{DF})

In the top panel of Figure 1 we show the stellar mass TFR for our sample. There is a noticeable transition at a stellar mass of $\log M_*/M_\odot \cong 9.5$. Above this mass, all galaxies in our sample are on the local TFR. Below this mass, galaxies may or may not lie on the local TFR, with the galaxies falling off tending to display systematically high measurements of σ_g . We posit that $\log M_*/M_\odot \cong 9.5$ marks an important stellar mass associated with the stabilization and formation of a disk. We will refer to this mass as “the mass of disk formation”, M_{df} .

In Figure 1 we separate our sample into 3 bins, motivated by their location on the TFR. We define these populations as high mass ($\log M_*/M_\odot > 9.5$) disks (on the TFR; black triangles), low mass ($\log M_*/M_\odot < 9.5$) ordered ($\sigma_g/V_{\text{rot}} < 1$) disks (on the TFR; blue circles), and low mass ($\log M_*/M_\odot < 9.5$) disordered ($\sigma_g/V_{\text{rot}} > 1$) systems (scattering to low V_{rot} from the TFR; red diamonds). This notation will be continued for successive plots.

We compare the slope in the TFR, $\log V_{\text{rot}} \propto \alpha \log M_*$, with a local sample ($z < 0.1$) of 189 disk galaxies from SDSS (Reyes et al. 2011), who find a value of $\alpha = 0.278 \pm 0.13$ over a mass range $9.0 < \log M_*/M_\odot < 11.0$. We refer to this relation as the TF “ridgeline” and mark it and its extrapolation to lower stellar masses in our TF plots. The high and low mass disks in our sample are well fit by the local ridgeline.

In the middle panel of Figure 1 we plot M_* versus σ_g . As mentioned previously, σ_g integrates unresolved velocity gradients in our systems, probing disordered components to the velocity field. The subset of galaxies that fall short of the Tully-Fisher ridgeline (red points) exhibit higher integrated velocity dispersions than the galaxies on the ridgeline at similar stellar mass.

As shown in K07 and K12, combining both the velocity dispersion and rotation velocity into a new kinematic parameter, $S_K = \sqrt{KV_{\text{rot}}^2 + \sigma_g^2}$, establishes a relatively tight relation. In the bottom panel of Figure 1 we plot S_K versus M_* for $K=0.5$. The choice of $K=0.5$ is motivated by virial arguments for a spherically symmetric tracer distribution (see Weiner et al. 2006a). Combining both the velocity dispersion and rotation velocity into $S_{0.5}$ re-establishes a tight analogue to the TFR, independent of morphology and coincident with the Faber-Jackson relation (K07, K12).

As expected, for galaxies in our sample, the residual from the local TF ridgeline is a strong function of σ_g/V_{rot} . In Figure 2 we demonstrate this correlation, demarcating the region where ordered disk galaxies fall (i.e. those on the TFR) would fall. We will use σ_g/V_{rot} as a proxy for the location of a galaxy on the TFR plot (Figure 1, top).

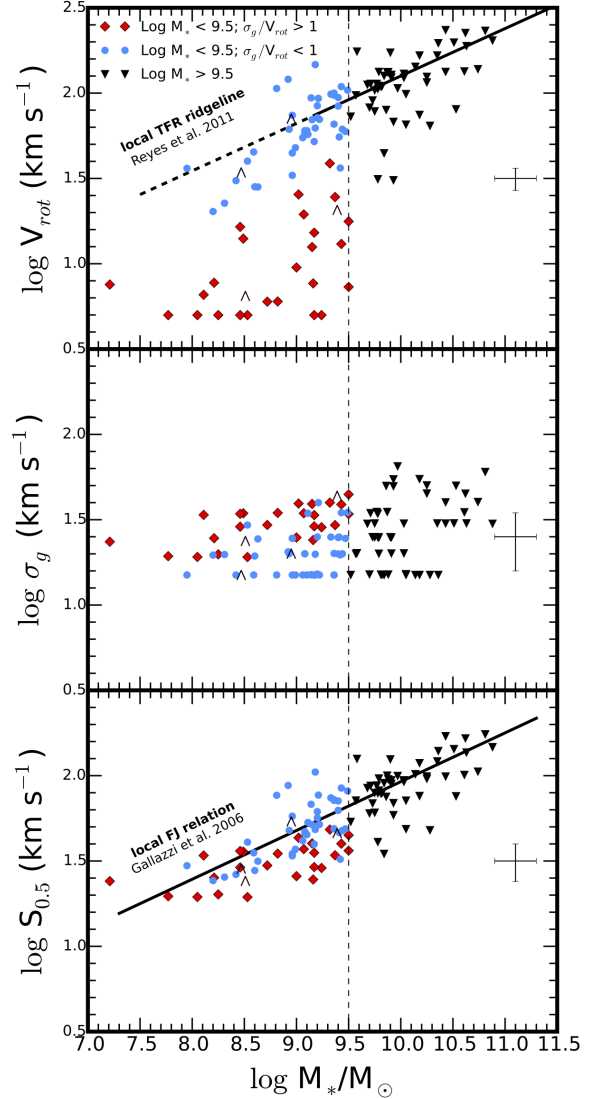


Figure 1. (a) The stellar mass Tully-Fisher relation for the K07/K12 sample of galaxies at $0.1 < z < 0.375$ is shown. Below a stellar mass of $\log M_*/M_\odot \cong 9.5$, there is significant scatter to low V_{rot} (red points). The local TFR (Reyes et al. 2011) (black line), adjusted for a Chabrier (2003) IMF, and its extrapolation to lower stellar masses (dashed line) is shown. b) For the same galaxies the integrated gas velocity dispersion, a measure of disordered motions, is shown versus stellar mass. c) Accounting for both ordered and disordered motions in the $S_{0.5}$ - M_* relation results in a relatively tight scaling, coincident with the local Faber-Jackson relation from Gallazzi et al. (2006). Galaxies are color/shape coded according to whether they are on the TF ridgeline and whether they have high or low stellar mass. This coding is repeated in other plots in the paper. The rotation velocities for the four galaxies with carats are not inclination corrected due to their highly uncertain inclination.

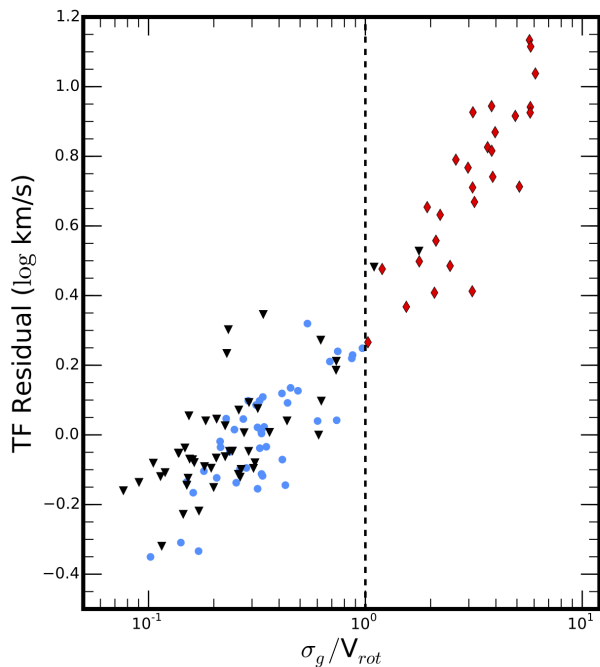


Figure 2. The residual from the local Tully-Fisher ridge line (Reyes et al. 2011) is plotted versus the ratio of disordered to ordered motions (σ_g/V_{rot}). As expected from K07 and K12, these quantities trace each other well. We use σ_g/V_{rot} to quantify the location of a galaxy on the TFR in the remainder of this paper.

4 MORPHOLOGY AND GAS KINEMATICS

In Figure 3 we reproduce the TFR in Figure 1, but replace the data points with HST V + I-band color images. Upon visual inspection we note distinct morphological characteristics among the regions of this plot identified in Figure 1. The galaxies with stellar masses higher than $\log M_*/M_\odot \cong 9.5$ exhibit extended disk-like morphologies. Galaxies with stellar masses $\log M_*/M_\odot < 9.5$ that are rotation dominated ($\sigma_g/V_{rot} < 1$) also show disk morphology, although they are less extended than the higher mass systems. Galaxies that fall below the TF ridgeline have dispersion dominated kinematics ($\sigma_g/V_{rot} > 1$) and show irregular or compact morphologies.

In Figure 4, we show two representative galaxies from each of the three defined regions in Figure 1 (from left to right): (1) low mass dispersion dominated galaxies which have compact morphology and irregular asymmetric features, (2) low mass rotationally supported galaxies which have characteristic morphologies of disks: they are more or less symmetric and elongated, and (3) high mass ordered galaxies which have similar disk-like morphologies.

These trends were noted by visual inspection in previous work (K07). We will now demonstrate that gas phase kinematics are related to quantitative galaxy morphology by comparing σ_g/V_{rot} (ratio of disordered to ordered motions)

to quantitative morphological indices (Gini coefficient, concentration, asymmetry). As described in the rest of this section, we find that the galaxies which fall on the Tully-Fisher ridgeline tend to exhibit low values of asymmetry, concentration, and Gini. In addition, they tend to have larger sizes consistent with the disk size-mass relation. Kinematically ordered galaxies ($\sigma_g/V_{rot} < 1$) at both low and high mass are consistent with being drawn from identical parent distributions for these indices. Galaxies which are kinematically disordered ($\sigma_g/V_{rot} > 1$) and fall from the TFR ridgeline tend to exhibit quantitative morphologies characteristic of disturbed or compact systems (high asymmetry, concentration and Gini) and are statistically distinct from the galaxies on the TF ridgeline. Below we detail these findings.

The top panel in Figure 5 shows the asymmetry index versus σ_g/V_{rot} for our galaxy sample. Low mass disordered galaxies (red diamonds) on average have a higher distribution in asymmetry than the galaxies with ordered kinematics which lie on the TF ridgeline (blue circles and black triangles). The asymmetry index is distributed with an average and standard deviation 0.18 ± 0.06 for low mass disordered systems and 0.11 ± 0.06 and 0.11 ± 0.04 for the low and high mass ordered systems, respectively. We run a two-sample Kolmogorov-Smirnov (K-S) test to determine the probability that the three distributions in asymmetry are drawn from identical parent distributions. The p-value returned from the K-S test represents the probability that data drawn from identical parent distributions would be as disparate as observed. The K-S test between the low and high mass ordered populations yields a p value of 0.77, indicating a high probability of being drawn from identical parent distributions. However, the K-S tests between the low mass disordered galaxies and the high/low mass ordered distributions yield near zero probabilities of being identical ($p = 10^{-5}$ and 10^{-4} , for comparisons with high and low mass ordered samples, respectively.)

The second panel in Figure 5 shows the Gini coefficient versus σ_g/V_{rot} . The disordered low mass population of galaxies exhibits a trend towards higher values of Gini. Average values of Gini increase from $G = 0.48 \pm 0.04$ and 0.48 ± 0.09 for the low and high mass ordered systems, respectively, to $G = 0.52 \pm 0.04$ for the disordered low mass systems. The K-S test between the ordered populations yields a p value of 0.48, while the dispersion dominated systems are unique compared with either distribution of ordered galaxies ($p = 10^{-5}$). While statistically significant, the relative change in Gini is small, reflecting the fact that even disk galaxies exhibit a level of non-uniformity (i.e. spiral features and clumpy star-formation). In large heterogeneous samples of galaxies the range of the Gini coefficient is relatively small (e.g. Lotz et al. 2008; Peth et al. 2015), with a floor at a value of around 0.40 for the most uniform galaxies and a peak value of only 0.65. In relation to this small range, a change of 0.04 reflects a non-negligible difference in galaxy type.

The third panel of Figure 5 shows the concentration index versus σ_g/V_{rot} . Similar to the Gini coefficient, kinematically disordered systems typically display higher values of

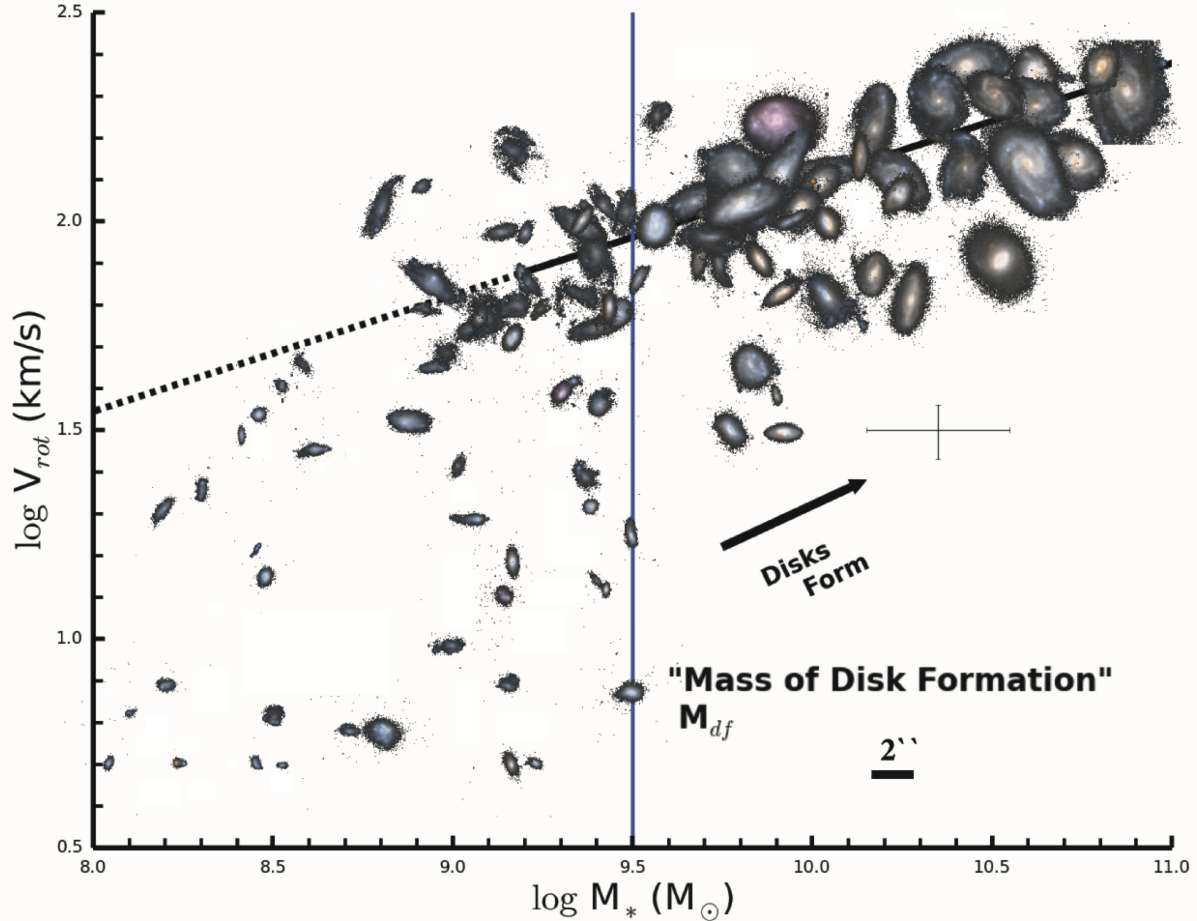


Figure 3. The Tully-Fisher relation for a morphologically unbiased sample of blue galaxies over $0.1 < z < 0.375$. V and I-band Hubble images are shown in place of points. A $2''$ size scale is included for reference. The local TFR from Reyes et al. (2011) is shown as a solid line and is extrapolated to lower masses with a dotted line. Galaxies with stellar masses $\log M_* \gtrsim 9.5 M_\odot$ fall on the TFR and on average have disk-like morphologies. Below this mass, a galaxy may or may not have formed a disk. We therefore call this mass the “mass of disk formation” (M_{df}). Low mass galaxies which fall from the TFR appear less extended and more irregular than the counterpart galaxies on the TFR. To make the figure manageable, a surface brightness cut on the images was selected based on the higher mass galaxies. This cut leads to a few of the low mass galaxies appearing smaller on this image than their true extent.

concentration. The concentration index increases from 0.51 ± 0.09 and 0.53 ± 0.07 for the low and high mass ordered systems, respectively, to 0.65 ± 0.12 for the disordered low mass systems. The K-S test between the ordered populations yields a p value of only 0.02, due to the large scatter in the low mass ordered distribution. The p value between the low mass disordered distribution and the ordered distributions is once again near zero ($p = 10^{-5}$).

We now examine the correlation between size with disordered motions in our sample. We use the HST V-band half-light radius R_{50} as measured using GIM2D. The low mass dispersion dominated galaxies have a mean value of $R_{50}/\text{kpc} = 1.8 \pm 1.2$ rms. The low and high mass ordered

systems are close to a factor of 2 larger, 3.1 ± 1.5 and 4.5 ± 2.0 kpc, respectively. To account for the well known mass dependence on size, we examine residuals from the SDSS DR7 median fit to the disk mass-size relation (Equation 3 in Dutton et al. 2011). In the bottom panel of Figure 5 we plot the log residual from the size mass relation ($\log(R_{50}/R_{50, RM})$) versus σ_g/V_{rot} . The ordered galaxies in our sample are distributed around the relation with an average scatter of 0.22 dex, consistent with the intrinsic width of the relation. The residuals for the dispersion dominated systems are centered 0.15 dex below the relation, although there are a few outliers that lie on or above the relation. At a given mass, the dis-

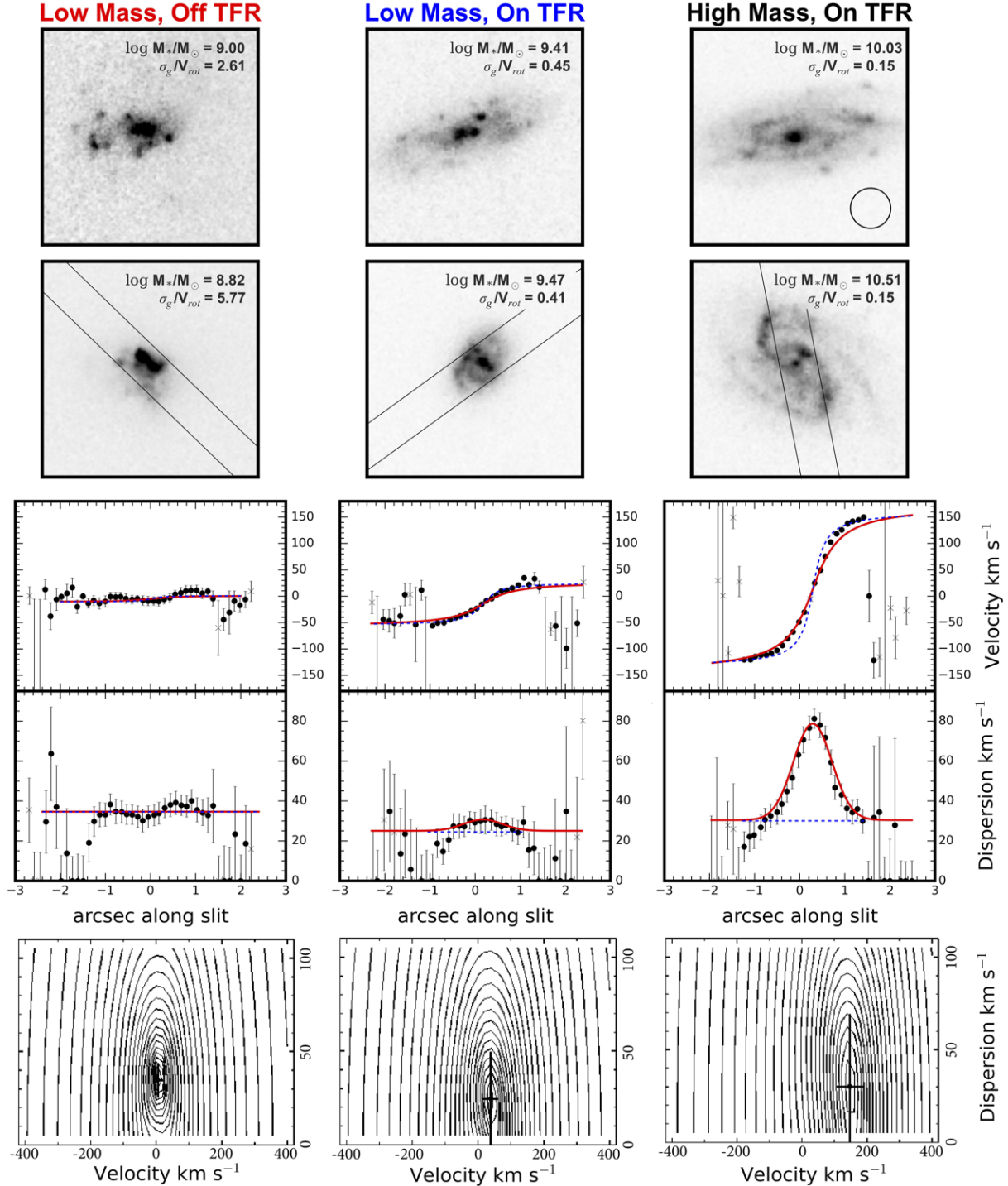


Figure 4. Upper Panels: HST V-band images of characteristic galaxies in the three regions of the TFR, Figure 1 (top). Individual images are 4'' on a side. Outer low surface brightness features are present but not apparent in the images of the low mass images due to the contrast settings chosen. The black circle represents a seeing of 0.75''. Top Left: Low mass galaxies which scatter to low V_{rot} from the TFR are shown. These exhibit compact emission with irregular asymmetric features. Top Middle: Low mass galaxies on the TFR are shown. They exhibit disk-like morphologies characterized by symmetric and elongated intensity distributions. Top Right: High mass ordered galaxies on the TFR are shown. They also exhibit more extended disk-like morphologies. Lower Panels: Example kinematic fits are shown for the three galaxies in the second row. Filled circles were used in the fitting routine, while the crosses were rejected. The blue dashed line is the intrinsic model and the red curve is the seeing blurred model which is fit to the data. For galaxies with rotation gradients, the seeing creates a classic artificial central peak in the velocity dispersion profile and slightly lowers the rotation velocity. Bottom Panels: χ^2 contours for the model parameters.

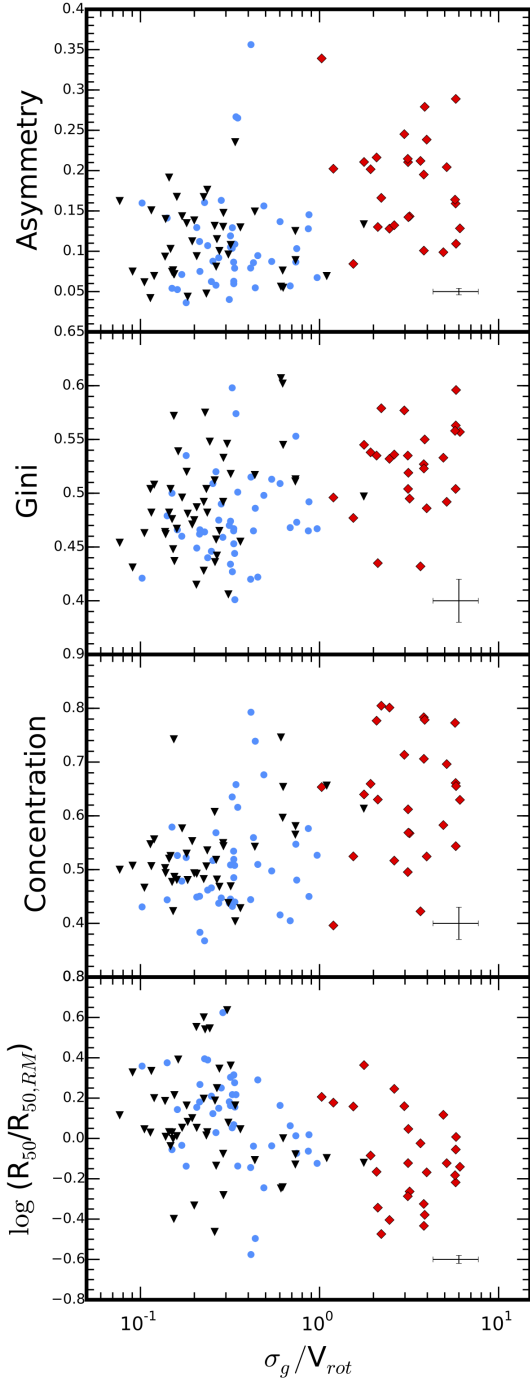


Figure 5. Quantitative morphological indices and V-band half-light radius (R_{50}) are shown as a function of kinematics for the galaxies in our sample. The bottom panel shows the log residuals from the SDSS g+r derived disk mass-size relation (RM; Dutton et al. 2011). The quantity σ_g/V_{rot} measures the relative contributions from disordered motions and ordered rotation. Galaxies which scatter to low V_{rot} off of the TF ridgeline (red diamonds) are on average more asymmetric, have higher Gini and concentration values, and are smaller than galaxies on the TF ridgeline (blue circles for low mass and black triangles for high mass).

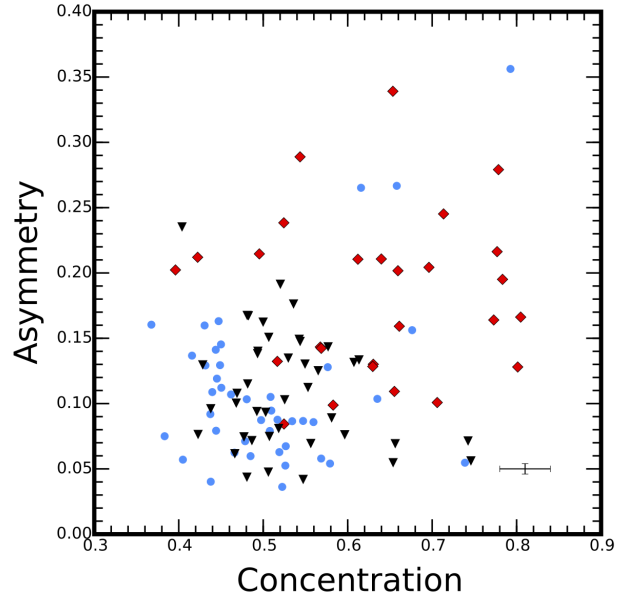


Figure 6. In the concentration-asymmetry plane, the high and low mass systems (black triangles and blue circles, respectively) are relatively localized to low asymmetry and concentration values. Low mass dispersion dominated galaxies (red diamonds) tend to scatter to larger values of both asymmetry and concentration.

person dominated systems tend to be smaller than expected from the radius-mass relation.

In the concentration-asymmetry plane (Figure 6) these differences become more apparent, with both the low and high mass ordered galaxies occupying relatively narrow regions of low asymmetry and concentration. The dispersion dominated systems, however, tend to exhibit markedly high scatter in this plane, tending towards higher values of both concentration and asymmetry.

In summary: The ordered systems in our sample display quantitative indices characteristic of disks: low asymmetry and low concentration. Kinematically disordered galaxies on the other hand exhibit concentrated emission with asymmetric features, statistically distinct from their ordered counterparts.

5 COMPARISON WITH PREVIOUS STUDIES

5.1 Local Universe

Large local studies of the TFR have primarily focused on massive disk galaxies with $\log M_*/M_\odot \gtrsim 9.5$ (e.g. Verheijen 2001; Pizagno et al. 2007; Courteau et al. 2007; Bershadsky et al. 2010; Reyes et al. 2011). We find that the majority of star-forming galaxies above this mass are morphologically disk-like and the TFR is well behaved. In fact, the only populations of dispersion dominated systems at high stellar masses in the local Universe are the relatively rare and

interaction induced (U)LIRGs systems (e.g. Arribas et al. 2014) and merging galaxies (e.g. the HI Rogues Gallery of Hibbard et al. 2001).

The TFR for $\log M_*/M_\odot < 9.5$ is less well-studied, especially for a morphologically unbiased sample. Furthermore, velocity dispersion is not frequently measured. Integrated line widths are often used as a proxy for the rotation velocity, with corrections assumed for anomalous contributions from random motions.

Most TFR studies of dwarf galaxies have focused on gas dominated systems ($M_g \geq M_*$). These galaxies typically show large residuals from the TFR to lower masses at a given rotation velocity, in the opposite direction to our sample. A tight baryonic Tully-Fisher relation is established once gas masses are included (McGaugh 2005) and it has been well calibrated for a local sample of gas-dominated galaxies (e.g. Stark et al. 2009).

For local dwarf galaxies with both σ_g and V_{rot} measured, evidence for a luminosity dependence on V/σ_g has been long established (e.g. Mateo 1998). This trend is to be expected even for galaxies on the TFR, if we assume that σ_g is independent of mass and V_{rot} declines with mass. When available, though, resolved kinematics of irregular or compact dwarf systems typically show complex velocity fields which depart from a regularly rotating thin disk (e.g. Barton et al. 2001; Kannappan et al. 2002; Vaduvescu et al. 2005). For instance, the well studied SMC ($M_*/M_\odot \sim 10^{8.7}$) and LMC ($M_*/M_\odot \sim 10^9$) are both rotationally supported in their stellar and neutral gaseous components ($V/\sigma \sim 3$), while the kinematics of the smallest local dI systems, traced through neutral HI gas, typically showing no signs of rotation (e.g. Young et al. 2003).

Recent surveys of HI in the local volume have helped further characterize the dynamics of dwarfs, e.g. THINGS (Walter et al. 2008), FIGGS (Begum et al. 2008b), VLA-ANGST (Ott et al. 2012) and LITTLE THINGS (Hunter et al. 2012). These surveys find mixed evidence among dwarf galaxies for both the existence of (i) rotationally supported disks (e.g. Begum et al. 2008a; Walter et al. 2008) and (ii) systems with thick disks or high/dominant contributions of dispersion (e.g. Roychowdhury et al. 2010; Ott et al. 2012).

The current data for resolved ionized gas kinematics in low mass galaxies is more limited. Interest in actively star-forming blue compact dwarfs (BCD) has led to measurements of velocity fields for a relatively large sample (~ 100) of these systems, usually in HI (e.g. van Zee et al. 1998, 2001; Thuan et al. 2004). Star-bursting systems, of which BCDs are a subset, make up close to 5% of the population of local dwarf galaxies (Lee et al. 2009). The origin of the compactness and late stage star-formation in the low mass ($\log M_*/M_\odot \sim 7.0 - 9.6$; Zhao et al. 2013) BCDs is up for debate. Recent HI investigations suggest high fractions of kinematically disturbed disks ($\sim 50\%$), although only a handful of systems fall short of the baryonic Tully-Fisher relation (Lelli et al. 2014). The ionized velocity fields are often found to exhibit high or dominant contributions from dispersion as well (e.g. Pérez-Gallego et al. 2011).

One of the largest surveys of resolved ionized gas kine-

matics in local galaxies is the GHASP survey (Gassendi H α Survey of Spirals; Epinat et al. 2008, 2010). The GHASP survey selection was focused on galaxies with both spiral and irregular morphologies, although most of the more luminous galaxies display characteristic disk morphologies. The GHASP survey samples a wide range in stellar mass $9.0 < \log M_*/M_\odot < 11.7$ (Epinat et al. 2008). The TFR for a subset of galaxies is found to be relatively tight down to $M_K = -18$ or $\log M_* = 8.0 M_\odot$ (Torres-Flores et al. 2011). While galaxies with large non-circular motions and corresponding rotation curve asymmetries show the largest scatter from the TF relation, to both low V_{rot} and low luminosity, the scatter is small compared to the dispersion dominated systems in our sample. Aside from a few outliers, no large break to low rotation velocity was found in the TFR for the GHASP sample. This may be due to a combination of both small sample sizes at masses $\log M_*/M_\odot < 9.5$ (9 galaxies) and/or selection functions for rotating galaxies playing a role in constructing the stellar mass TFR. The σ/V for these 9 low mass galaxies ranges between 0.1 - 0.7 (i.e. all would be kinematically ordered in this paper). On visual inspection of their optical morphologies in NED, we note that seven of these galaxies appear to have disk morphologies, with the presence of spiral arms in most cases. The low σ/V in these galaxies is consistent with the picture presented in this paper, that disk morphologies indicate ordered kinematics. Two of the galaxies (UGC 5721, UGC 10757) do appear to have disturbed morphologies, so it is interesting to note that their σ/V is still less than 1 (0.16 and 0.35, respectively). The mean velocity dispersion for the GHASP sample is $25 \pm 5 \text{ km s}^{-1}$, typical of local disks in general. This level of dispersion is expected for a combination of the thermal broadening from H atoms ($T \sim 10^4 \text{ K}$; $\sim 10 \text{ km s}^{-1}$) and internal turbulence of HII regions ($\sim 20 \text{ km s}^{-1}$; Shields 1990). These measurements are comparable to the mean velocity dispersions for our ordered disks ($21.0 \pm 8.1 \text{ km s}^{-1}$) and slightly lower than our systems with more disturbed kinematics ($34 \pm 7.3 \text{ km s}^{-1}$). For the few compact rotators in GHASP we ran mock tests (see Appendix A for an example with galaxy UGC 528) to ensure that we could accurately recover their rotation if they were in our sample at $z \sim 0.2$. The results of these tests indicate that if these galaxies were included in our sample we would recover their rotating disks.

Our understanding of the ionized kinematics of dwarf galaxies at low redshifts will substantially increase in the near future with ongoing and upcoming Integral Field Spectroscopy (IFS) surveys. The CALIFA ($0.005 < z < 0.03$, $R \sim 850\text{-}1650$; $N \sim 600$), SAMI ($z < 0.12$, $R \sim 1700\text{-}4500$; $N \sim 3400$) and MaNGA ($z \sim 0.03$; $R \sim 2000$; $N \sim 10,000$) surveys will provide velocity fields for large ensembles of local low mass galaxies. First results from CALIFA (García-Lorenzo et al. 2015) have reported that about half of the galaxies in their sample ($8.5 < \log M_*/M_\odot < 11.5$) have structure in their velocity fields which departs from a rotating disk. However, resolved velocity dispersions were not measured in this study and the relatively coarse spectral resolution ($R \sim 1200$) may not allow for measurements of the dispersion at the differences outlined in this paper. First results from

SAMI show a large fraction of both low and high mass local galaxies falling to low V_{rot} from the TFR (Cortese et al. 2014). The SAMI survey improves upon the GHASP sample with a large coverage of low mass systems, pushing down to stellar masses $\log M_*/M_\odot \sim 8$. Below a stellar mass $\log M_*/M_\odot \cong 9$, they find a precipitous trailing of galaxies from the well-defined 1 R_e TF relation (Yegorova & Salucci 2007). High spectral resolution in the red band (6300-7400 Å, $R \sim 4500$) allow measurements of velocity dispersions. A tight scaling relation (M_*-S_K) is established once they account for the average measured velocity dispersion, similar to previous findings at high redshift (Weiner et al. 2006b; Kassin et al. 2007; Puech et al. 2010). The SDSS-III MaNGA survey will provide extensive additional coverage of this low mass regime, with a flat selection distribution down to a stellar mass of $10^9 M_\odot$ and sampling out to at least 1.5 times the effective radius (R_e) (Bundy et al. 2015).

In summary, when studied in large numbers, local studies of the TFR have been biased towards massive disk galaxies and moreover will often not have the spectral resolution to resolve velocity dispersion. When resolved gas phase kinematics are available in low mass galaxies, complex velocity fields are often found in both neutral and ionized gas. The local TFR for dwarf galaxies will be expanded upon in the upcoming years, with surveys probing kinematics in ionized gas to low stellar masses in unprecedented numbers. Early results indicate an increase in complexity in the resolved 2D velocity fields of these low mass galaxies.

5.2 Low-Intermediate Redshift

Due primarily to sensitivity limits, there have been few studies of the kinematics in more distant ($z > 0.1$) dwarf galaxies. Furthermore, most studies do not measure resolved velocity dispersions and do not include irregular or compact galaxies.

Using deep 8 hour DEIMOS exposures, Miller et al. (2014) constructed the stellar mass TFR for half of their sample ($N = 41$) of dwarf galaxies ($7 < \log M_*/M_\odot < 9$) out to $z = 1$, demonstrating that at least a fraction of dwarf galaxies are settled into rotationally supported systems at intermediate redshift. The remaining galaxies were either missing emission or were too small to reliably resolve rotation.

Recently, interest in dispersion dominated galaxies at high redshift (e.g. Law et al. 2009; Förster Schreiber et al. 2009) has motivated searches for high dispersion low redshift analogs. These studies typically select highly star-forming systems and find complex kinematics with low V/σ_g compared to local disk galaxies (e.g. Gonçalves et al. 2010; Amorín et al. 2012; Green et al. 2014).

Compact Lyman Break analogues (LBA) are an example of such a selection. LBAs are highly star-forming galaxies at $z \sim 0.2$, selected from their high GALEX NUV luminosity (Heckman et al. 2005). Although these systems have slightly higher stellar masses $9.5 \leq \log M_*/M_\odot \leq 10.7$ than the break in our sample, they exhibit morphologies and kinematics which are similar to some of our more compact dwarf galaxies. Gonçalves et al. (2010) report on AO-assisted IFS observa-

tions of 19 compact LBAs at $z \sim 0.2$ with stellar masses near our transition mass, $9.1 < \log M_*/M_\odot < 10.7$. They find a very high contribution of disordered motion in these rare systems ($\sigma_g \sim 70 \text{ km s}^{-1}$) and evidence that disk-like structure is more common in high mass LBAs. Similarly, Green et al. (2014) measured H α kinematics for 67 extremely star-forming systems down to a stellar mass of $10^9 M_\odot$ and found that one fifth of their sample shows no signs of rotation. The rotating disk galaxies in their sample fall on the TFR while still exhibiting values of V/σ_g lower than local disks, comparable to dynamically hot high redshift galaxies. The dispersion dominated galaxies $V/\sigma_g \leq 1$ in both the intermediate redshift IFS samples have typical stellar masses above our observed mass of disk formation ($\log M_{df}/M_\odot \sim 9.5$). Although the unique selections (e.g. high star-formation, high surface mass density) for these samples are not necessarily representative, they do demonstrate the important contribution of σ_g to the kinematics in active systems.

At high redshifts ($1.5 < z < 3$), complex velocity fields and thick disks with high velocity dispersions are ubiquitous in the samples currently available in the literature (e.g. Law et al. 2009; Förster Schreiber et al. 2009; Wisnioski et al. 2015). A stellar mass dependence on the relative contributions of σ_g and V_{rot} appears to exist, although beam smearing (see Appendix) may provide the enhanced dispersion in some of the the smallest systems (Newman et al. 2013). Kinematic data for low mass galaxies at these redshifts is currently limited. The advent of high sensitivity near-IR instruments (e.g. MOSFIRE, KMOS) will soon provide large samples of kinematics for galaxies with low stellar masses.

6 CONCLUSIONS

We study the stellar mass Tully-Fisher relation (TFR; stellar mass versus rotation velocity) for a morphologically blind sample of emission line galaxies in the field. The galaxies are at a redshift of ~ 0.2 , or a lookback time of about 2 Gyrs, and therefore we expect little evolution from the local TFR.

We report on a transition mass in the TFR which we call the “mass of disk formation,” M_{df} . This mass separates galaxies which always form disks (masses greater than M_{df}) from those which may or may not form disks (masses less than M_{df}). For $M_* > M_{df}$, all galaxies in our sample are settled onto the local TFR. However, for $M_* < M_{df}$, galaxies can either lie on the TFR or scatter off of it to low rotation velocity. The galaxies which scatter off have higher disordered motions, as measured through integrated gas velocity dispersions (σ_g). Moreover, we find that galaxies on the TFR are morphologically distinct from those which scatter off. The quantitative morphologies of galaxies on the relation are on average less asymmetric and concentrated than those galaxies which scatter off.

We perform mock observations of the 3D kinematics of local galaxies to investigate how well we are able to recover the rotation velocity of the smallest galaxies in our sample.

These simulations show that we are able to recover rotation, if present, in the smallest galaxies in our sample.

ACKNOWLEDGEMENTS

The authors would like to thank the anonymous referee who provided useful suggestions that improved this manuscript. RCS gratefully acknowledges support through a grant from the STScI JDF. This research has made use of the Fabry Perot database, operated at CeSAM/LAM, Marseille, France. The authors also acknowledge NSF grants AST 95-29098 and 00-71198 to UC Santa Cruz. RCS would like to thank A. Dutton for helpful comments. We wish to extend thanks to those of Hawaiian ancestry on whose sacred mountain we are privileged guests.

REFERENCES

- Abraham, R. G., Valdes, F., Yee, H. K. C., & van den Bergh, S. 1994, *ApJ*, 432, 75
- Abraham, R. G., Tanvir, N. R., Santiago, B. X., et al. 1996, *MNRAS*, 279, L47
- Abraham, R. G., van den Bergh, S., & Nair, P. 2003, *ApJ*, 588, 218
- Amorín, R., Vílchez, J. M., Hägele, G. F., et al. 2012, *ApJ*, 754, L22
- Arribas, S., Colina, L., Bellocchi, E., Maiolino, R., & Villar-Martín, M. 2014, *A&A*, 568, A14
- Barton, E. J., Geller, M. J., Bromley, B. C., van Zee, L., & Kenyon, S. J. 2001, *AJ*, 121, 625
- Begeman, K. G. 1987, Ph.D. Thesis,
- Begum, A., Chengalur, J. N., Karachentsev, I. D., & Sharina, M. E. 2008, *MNRAS*, 386, 138
- Begum, A., Chengalur, J. N., Karachentsev, I. D., Sharina, M. E., & Kaisin, S. S. 2008, *MNRAS*, 386, 1667
- Bell, E. F., & de Jong, R. S. 2001, *ApJ*, 550, 212
- Bell, E. F., Papovich, C., Wolf, C., et al. 2005, *ApJ*, 625, 23
- Bershady, M. A., Verheijen, M. A. W., Swaters, R. A., et al. 2010, *ApJ*, 716, 198
- Bertin, E., & Arnouts, S. 1996, *A&AS*, 117, 393
- Bothwell, M. S., Kennicutt, R. C., & Lee, J. C. 2009, *MNRAS*, 400, 154
- Brooks, A. M., Governato, F., Quinn, T., Brook, C. B., & Wadsley, J. 2009, *ApJ*, 694, 396
- Bundy, K., Ellis, R. S., Conselice, C. J., et al. 2006, *ApJ*, 651, 120
- Bundy, K., Bershady, M. A., Law, D. R., et al. 2015, *ApJ*, 798, 7
- Cannon, J. M., McClure-Griffiths, N. M., Skillman, E. D., & Côté, S. 2004, *ApJ*, 607, 274
- Catinella, B., Kauffmann, G., Schiminovich, D., et al. 2012, *MNRAS*, 420, 1959
- Chabrier, G. 2003, *The Publications of the Astronomical Society of the Pacific*, 115, 763
- Cortese, L., Fogarty, L. M. R., Ho, I.-T., et al. 2014, *ApJ*, 795, L37
- Courteau, S., Dutton, A. A., van den Bosch, F. C., et al. 2007, *ApJ*, 671, 203
- Covington, M. D., Kassin, S. A., Dutton, A. A., et al. 2010, *ApJ*, 710, 279
- Davis, M., Guhathakurta, P., Konidaris, N. P., et al. 2007, *ApJ*, 660, L1
- Davies, R., Förster Schreiber, N. M., Cresci, G., et al. 2011, *ApJ*, 741, 69
- De Rossi, M. E., Tissera, P. B., & Pedrosa, S. E. 2012, *A&A*, 546, A52
- Dutton, A. A., van den Bosch, F. C., Dekel, A., & Courteau, S. 2007, *ApJ*, 654, 27
- Dutton, A. A., van den Bosch, F. C., Faber, S. M., et al. 2011, *MNRAS*, 410, 1660
- Elmegreen, B. G., & Burkert, A. 2010, *ApJ*, 712, 294
- Epinat, B., Amram, P., & Marcelin, M. 2008, *MNRAS*, 390, 466
- Epinat, B., Amram, P., Balkowski, C., & Marcelin, M. 2010, *MNRAS*, 401, 2113
- Faber, S. M., Phillips, A. C., Kibrick, R. I., et al. 2003, *Proc. SPIE*, 4841, 1657
- Förster Schreiber, N. M., Genzel, R., Bouché, N., et al. 2009, *ApJ*, 706, 1364
- Gallazzi, A., Charlot, S., Brinchmann, J., & White, S. D. M. 2006, *MNRAS*, 370, 1106
- Garrido, O., Marcelin, M., Amram, P., & Boissin, O. 2003, *A&A*, 399, 51
- García-Lorenzo, B., Márquez, I., Barrera-Ballesteros, J. K., et al. 2015, *A&A*, 573, A59
- Gonçalves, T. S., Basu-Zych, A., Overzier, R., et al. 2010, *ApJ*, 724, 1373
- Green, A. W., Glazebrook, K., McGregor, P. J., et al. 2014, *MNRAS*, 437, 1070
- Heckman, T. M., Hoopes, C. G., Seibert, M., et al. 2005, *ApJ*, 619, L35
- Hibbard, J. E., van Gorkom, J. H., Rupen, M. P., & Schiminovich, D. 2001, *Gas and Galaxy Evolution*, 240, 657
- Hunter, D. A., Ficut-Vicas, D., Ashley, T., et al. 2012, *AJ*, 144, 134
- Kannappan, S. J., Fabricant, D. G., & Franx, M. 2002, *AJ*, 123, 2358
- Kassin, S. A., de Jong, R. S., & Weiner, B. J. 2006, *ApJ*, 643, 804
- Kassin, S. A., Weiner, B. J., Faber, S. M., et al. 2007, *ApJ*, 660, L35
- Kassin, S. A., Weiner, B. J., Faber, S. M., et al. 2012, *ApJ*, 758, 106
- Kirby, E. N., Bullock, J. S., Boylan-Kolchin, M., Kaplinghat, M., & Cohen, J. G. 2014, *MNRAS*, 439, 1015
- Kronberger, T., Kapferer, W., Schindler, S., & Ziegler, B. L. 2007, *A&A*, 473, 761
- Law, D. R., Steidel, C. C., Erb, D. K., et al. 2009, *ApJ*, 697, 2057
- Lee, J. C., Kennicutt, R. C., Jr., Funes, S. J. J. G., Sakai, S., & Akiyama, S. 2009, *ApJ*, 692, 1305
- Lehnert, M. D., Nesvadba, N. P. H., Le Tiran, L., et al. 2009, *ApJ*, 699, 1660
- Lelli, F., Verheijen, M., & Fraternali, F. 2014, *A&A*, 566,

- AA71
- Lemoine-Busserolle, M., & Lamareille, F. 2010, *MNRAS*, 402, 2291
- Lin, L., Koo, D. C., Weiner, B. J., et al. 2007, *ApJ*, 660, L51
- Lotz, J. M., Primack, J., & Madau, P. 2004, *AJ*, 128, 163
- Lotz, J. M., Madau, P., Giavalisco, M., Primack, J., & Ferguson, H. C. 2006, *ApJ*, 636, 592
- Lotz, J. M., Davis, M., Faber, S. M., et al. 2008, *ApJ*, 672, 177
- Mac Low, M.-M., & Ferrara, A. 1999, *ApJ*, 513, 142
- Masters, K. L., Springob, C. M., & Huchra, J. P. 2008, *AJ*, 135, 1738
- Mateo, M. L. 1998, *ARA&A*, 36, 435
- Mahajan, S., Drinkwater, M. J., Driver, S., et al. 2015, *MNRAS*, 446, 2967
- McConnachie, A. W. 2012, *AJ*, 144, 4
- McGaugh, S. S. 2005, *ApJ*, 632, 859
- Miller, S. H., Ellis, R. S., Newman, A. B., & Benson, A. 2014, *ApJ*, 782, 115
- Mo, H. J., Mao, S., & White, S. D. M. 1998, *MNRAS*, 295, 319
- Mortlock, A., Conselice, C. J., Hartley, W. G., et al. 2013, *MNRAS*, 433, 1185
- Navarro, J. F., & Steinmetz, M. 2000, *ApJ*, 538, 477
- Newman, J. A., Cooper, M. C., Davis, M., et al. 2013, *ApJS*, 208, 5
- Newman, S. F., Genzel, R., Förster Schreiber, N. M., et al. 2013, *ApJ*, 767, 104
- Ott, J., Stilp, A. M., Warren, S. R., et al. 2012, *AJ*, 144, 123
- Patil, A., D. Huard and C.J. Fonnesbeck. 2010. PyMC: Bayesian Stochastic Modelling in Python. *Journal of Statistical Software*, 35(4), pp. 1-81
- Pérez-Gallego, J., Guzmán, R., Castillo-Morales, A., et al. 2011, *MNRAS*, 418, 2350
- Peth, M. A., Lotz, J. M., Freeman, P. E., et al. 2015, *arXiv:1504.01751*
- Puech, M., Hammer, F., Flores, H., et al. 2010, *A&A*, 510, A68
- Pizagno, J., Prada, F., Weinberg, D. H., et al. 2005, *ApJ*, 633, 844
- Pizagno, J., Prada, F., Weinberg, D. H., et al. 2007, *AJ*, 134, 945
- Rampazzo, R., Plana, H., Amram, P., et al. 2005, *MNRAS*, 356, 1177
- Reyes, R., Mandelbaum, R., Gunn, J. E., Pizagno, J., & Lackner, C. N. 2011, *MNRAS*, 417, 2347
- Roberts, M. S., & Haynes, M. P. 1994, *ARA&A*, 32, 115
- Roychowdhury, S., Chengalur, J. N., Begum, A., & Karachentsev, I. D. 2010, *MNRAS*, 404, L60
- Shields, G. A. 1990, *ARA&A*, 28, 525
- Simard, L., Willmer, C. N. A., Vogt, N. P., et al. 2002, *ApJS*, 142, 1
- Somerville, R. S., & Primack, J. R. 1999, *MNRAS*, 310, 1087
- Stark, D. V., McGaugh, S. S., & Swaters, R. A. 2009, *AJ*, 138, 392
- Swaters, R. A., van Albada, T. S., van der Hulst, J. M., & Sancisi, R. 2002, *A&A*, 390, 829
- Swaters, R. A., Sancisi, R., van Albada, T. S., & van der Hulst, J. M. 2009, *A&A*, 493, 871
- Thuan, T. X., Hibbard, J. E., & Lévrier, F. 2004, *AJ*, 128, 617
- Torres-Flores, S., Epinat, B., Amram, P., Plana, H., & Mendes de Oliveira, C. 2011, *MNRAS*, 416, 1936
- Tully, R. B., & Fisher, J. R. 1977, *A&A*, 54, 661
- Vaduvescu, O., McCall, M. L., Richer, M. G., & Fingerhut, R. L. 2005, *AJ*, 130, 1593
- van Zee, L., Skillman, E. D., & Salzer, J. J. 1998, *AJ*, 116, 1186
- van Zee, L., Salzer, J. J., & Skillman, E. D. 2001, *AJ*, 122, 121
- Vergani, D., Epinat, B., Contini, T., et al. 2012, *A&A*, 546, A118
- Verheijen, M. A. W. 2001, *ApJ*, 563, 694
- Walter, F., Brinks, E., de Blok, W. J. G., et al. 2008, *AJ*, 136, 2563
- Weiner, B. J., Willmer, C. N. A., Faber, S. M., et al. 2006a, *ApJ*, 653, 1027
- Weiner, B. J., Willmer, C. N. A., Faber, S. M., et al. 2006b, *ApJ*, 653, 1049
- Wisnioski, E., Förster Schreiber, N. M., Wuyts, S., et al. 2015, *ApJ*, 799, 209
- Yegorova, I. A., & Salucci, P. 2007, *MNRAS*, 377, 507
- Young, L. M., van Zee, L., Lo, K. Y., Dohm-Palmer, R. C., & Beierle, M. E. 2003, *ApJ*, 592, 111
- Zhao, Y., Gao, Y., & Gu, Q. 2013, *ApJ*, 764, 44

APPENDIX A: MODELING THE EFFECTS OF APPARENT SIZE ON MEASURING KINEMATICS

Reliably measuring resolved kinematics for a galaxy depends critically on its apparent size relative to the seeing, i.e. beam smearing (Begeman 1987). Atmospheric turbulence blurs together intrinsically spatially separate velocity gradients, leading to a smoothing of the rotation field and a boosted central velocity dispersion (e.g. Weiner et al. 2006a). ROTCURVE models the seeing and recovers rotation curves and average integrated gas velocity dispersions for galaxies with apparent sizes larger than the seeing (see examples in Weiner et al. 2006a). Overcoming beam smearing with galaxies whose intrinsic size is comparable to the seeing is challenging and has been addressed by several papers with respect to IFS measurements at high redshift (e.g. Epinat et al. 2010; Davies et al. 2011).

To understand the effects of beam smearing on our measurements we perform mock observations of observed velocity and dispersion maps for a nearby galaxy from the literature. In particular, we use Fabry-Perot observations of UGC 528 from the GHASP survey (Epinat et al. 2010). We determine the apparent galaxy size (defined as the extent of the line emission) at which the intrinsic rotation velocity

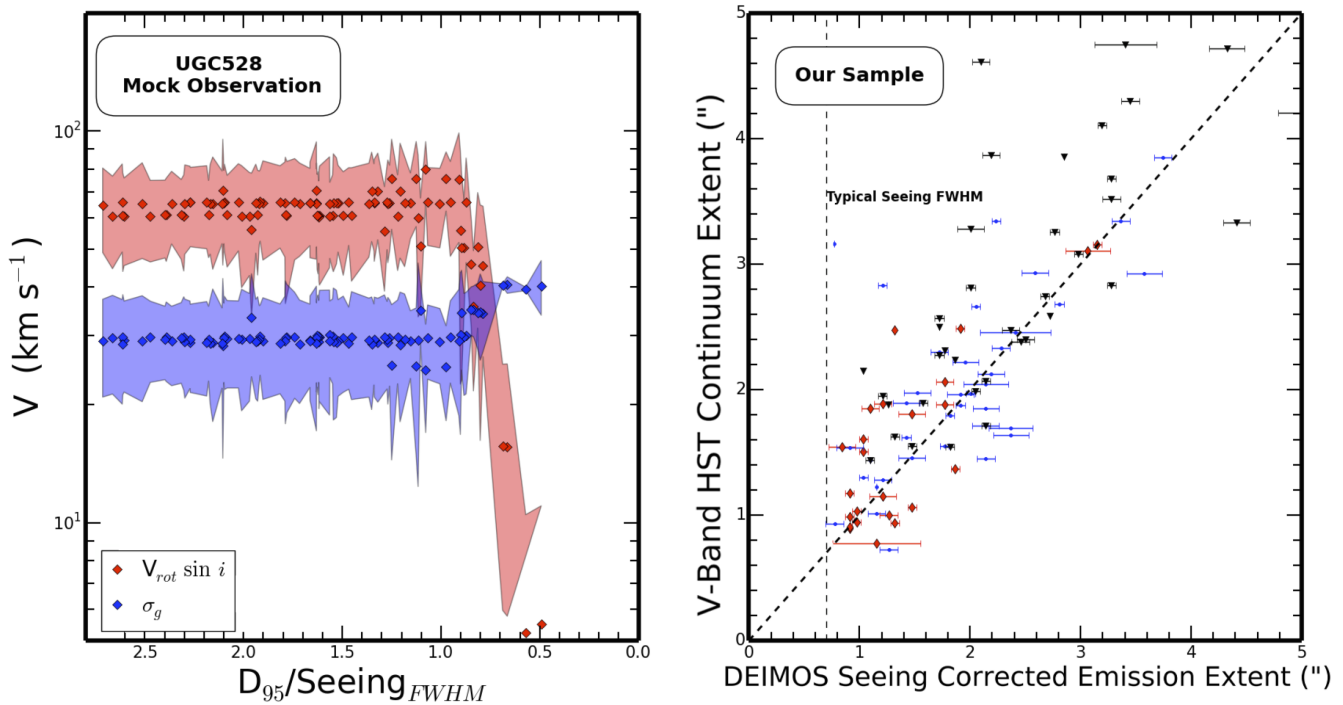


Figure A1. Left: Mock observations of UGC 528 at varying apparent sizes. The seeing is kept constant at $0.75''$ for all mock observations. We are able to recover the true rotation velocity and average gas velocity dispersion down to a diameter, $D_{95} = (0.87 \pm 0.06) \times \text{seeing}$. Right: Measurements of the continuum and emission line extent for the galaxies in our sample. The continuum extent is defined as $4 \times \sigma_{cont}$ of the intensity profile. For a Gaussian profile, this will equal D_{95} . For galaxy profiles with broader wings than a Gaussian, D_{95} will be larger than this value. The continuum is derived from the V-band image (rest B at $z = 0.2$) and should trace the young star forming regions. The seeing-corrected DEIMOS emission line extent is defined as $4 \times \sigma_{emission}$. The seeing for the observations in our sample ranged between $0.55''$ - $1.20''$. The number of galaxies for each bin in seeing are: $[0.55 - 0.70'']$ 26 galaxies, $[0.70 - 0.85'']$ 44 galaxies, $[0.85 - 1.0'']$ 35 galaxies, $[1.0 - 1.2'']$ 14 galaxies. The typical seeing for our sample is demarcated by the vertical black line. All of the galaxies in our sample are sufficiently large enough to reliably measure a rotation velocity, if present.

is no longer recovered under the observing conditions and instrumental set-up used by the DEEP2 Survey.

A1 Mock Observations of UGC 528

UGC 528 is a small rotating local spiral galaxy of Hubble Type SAB(rs)b (Garrido et al. 2003). It has a rotation velocity $V_{rot} \sin(i) \sim 60 \text{ km s}^{-1}$ and a relatively high average dispersion across its face of $\sigma_g = 26.0 \pm 9.6 \text{ km s}^{-1}$.

We build mock spectral cubes (3D: spatial \times spatial \times λ) from the available velocity, dispersion and flux maps. This allows us to perform mock observations for an arbitrary velocity sampling without needing to interpolate between slices. To do this, we first construct an empty cube with velocity sampling matching DEEP2, namely $\Delta v = 12.6 \text{ km s}^{-1}$ at $z = 0.2$. Next, using the flux, velocity and dispersion maps we fill the cube with model H α emission. For each spaxel in the map with valid velocity information we create a Gaussian line profile with a mean line of sight velocity V_{los} , dispersion σ_g and amplitude scaled to match the integrated flux. This cube is then projected from its original redshift to $z = 0.2$ by resizing the spaxel scale. Each slice in the cube is

then convolved with a 2D spatial Gaussian kernel (FWHM = $0.75''$) to simulate seeing.

A mock $1''$ wide slit is placed along the kinematic PA of the galaxy. From this we produce a mock spectrum using the DEEP2 pixel scales ($0.118''/\text{pixel}$, $0.33''/\text{pixel}$) and spectral resolution ($R \sim 5000$). Noise is added to the 2D spectrum to match the typical pixel to pixel S/N profiles of our faintest sources.

We create separate cubes in this manner, each time varying the spatial size to simulate different apparent sizes for UGC 528. The final product is a set of 100 mock observations of UGC 528 at $z = 0.2$ ranging in size 0.4 - $2.2''$ with a $0.018''$ step size. Each mock observation results in a 2D spectrum of the emission line for a given apparent size.

Next we run each of the mock spectra through ROTCURVE to measure kinematics. We fix the scale radius of UGC 528 in physical units to its true value of 0.6 kpc (Epinat et al. 2010). For reasonable values, we find that the chosen scale radius has little impact on the kinematic measurements, as was also found by Weiner et al. (2006a). We measure $V_{rot} \times \sin(i)$ and σ_g for each of the 100 mock spectra. The results of our test are demonstrated in Figure A1. As expected, at large intrinsic sizes relative to the see-

ing ($D_{95} > 1.5 \times \text{seeing}$) we are able to recover the intrinsic rotation and integrated dispersion well. As the mock observations reach closer to and beyond the scale of the seeing, we note that the measured rotation velocity decreases and the measured dispersion increases as expected. To quantify the scale at which this turnover occurs, we fit a simple change point model using PyMC (Patil, A., D. Huard and C.J. Fonnesbeck. 2010). The turnover to artificially low V_{rot} occurs at a scale of $D_{95}/\text{Seeing} = 0.87 \pm 0.06$. This error incorporates both the measurement error imposed by the slit (red shading in Figure A1, left) and the error in the fit to the model.

We conclude from these mock observations that we can reliably measure rotation velocities for the galaxies in our sample down to $D_{95}/\text{Seeing} = 0.87 \pm 0.06$.

A2 Emission sizes vs HST Continuum sizes

We now compare the intrinsic sizes of the galaxies in our sample to the size of the seeing. In the right panel of Figure A1 we plot the size of the galaxy in emission, tracing areas of star-formation, against the size in continuum, tracing the young stellar population. The Hubble sizes are measured from the HST V-Band images and the emission sizes are measured directly from the DEIMOS spectra. The observed emission lines ($\sigma_{em,obs}$) are broadened by the combined PSF of the instrument and the seeing (σ_{PSF}). We can recover the true extent of the emission line ($\sigma_{em,corr}$):

$$\sigma_{em,corr} = \sqrt{\sigma_{em,obs}^2 - \sigma_{PSF}^2} \quad (\text{A1})$$

For an approximate 1-D Gaussian profile, the diameter containing 95% of the flux will be 4 times this value. In reality, intrinsic emission profiles of galaxies will be broader than a Gaussian distribution and the value of $\sigma_{em,corr}$ is primarily determined by the profile of the core. A galaxy profile with broader wings than a Gaussian will have a D_{95} that is larger than that given by $4 \times \sigma_{em,corr}$. The HST V-band (rest B at $z \sim 0.2$) extent correlates well with the seeing-corrected emission line sizes (Figure A1, right). We demarcate the typical seeing size of $0.75''$.

The smallest galaxies in our sample reach down to seeing-corrected emission extents of $\sim 1.2''$ (or 1.6 times the typical seeing FWHM), well into the predicted regime for accurately recovering the kinematics (Figure A1; left panel). In conclusion, it is unlikely that our low mass dispersion dominated galaxies are dispersion-dominated because of beam-smearing.